Modeling the NIR-silhouette massive disk candidate in M 17

J. Steinacker, R. Chini, M. Nielbock, D. Nürnberger, V. Hoffmeister, J.-M. Huré, D. Semenov

A&A 456, 1013–1026 (2006)
DOI: 10.1051/0004-6361:20054312

Astronomy & Astrophysics

Modeling the NIR-silhouette massive disk candidate in M 17⋆

J. Steinacker[1,2], R. Chini[3], M. Nielbock[3], D. Nürnberger[4], V. Hoffmeister[3], J.-M. Huré[5,6,7], and D. Semenov[1]

[1] Max-Planck-Institut für Astronomie, Königstuhl 17, 69117 Heidelberg, Germany
e-mail: [stein;semenov]@mpia.de
[2] Astronomisches Rechen-Institut am Zentrum für Astronomie Heidelberg, Mönchhofstr. 12-14, 69120 Heidelberg, Germany
[3] Astronomisches Institut, Ruhr-Universität Bochum, 44780 Bochum, Germany
e-mail: [chini;nielbock;hoffmeister]@astro.rub.de
[4] European Southern Observatory, Casilla 19001, Santiago 19, Chile
e-mail: dnuernbe@eso.org
[5] ERA/L3AB/Observatoire Aquitain des Sciences de l'Univers, 2 rue de l'Observatoire, 33270 Floirac, France
e-mail: jean-marc.hure@obs.u-bordeaux1.fr
[6] Université Bordeaux 1, 351 cours de la Libération, 33405 Talence, France
[7] LUTh/Observatoire de Paris-Meudon (research associate), Place Jules Janssen, 92195 Meudon Cedex, France

Received 6 October 2005 / Accepted 23 May 2006

ABSTRACT

Aims. The physical properties of the massive disk candidate in the star-forming region M 17 are analyzed.
Methods. Making use of the rare configuration in which the gas and dust structure is seen in silhouette against the background radiation at $\lambda = 2.2$ μm, we determine the column density distribution from a high-resolution NAOS/CONICA image. The influence of scattered light on the mass determination is analyzed using 3D radiative transfer calculations. Further upper flux limits derived from observations with the Spitzer telescope at MIR wavelengths are used together with the NACO image to estimate the flux from the central object. For a range of stellar radii, stellar surface temperatures, and dust grain sizes, we apply three different models to account for the observed fluxes. The stability of the disk against self-gravitational forces is analyzed calculating the ratio of the gravitational acceleration by the central object and the disk, and the deviations from a Keplerian profile.
Results. We find that the column density is consistent with a central source surrounded by a rotationally symmetric distribution of gas and dust. The extent of the symmetric disk part is about 3000 AU, with a warped point-symmetrical extension beyond that radius, and therefore larger than any circumstellar disk yet detected. The modeling yields a radial density powerlaw exponent of −1.1 indicating a flat radial density distribution, and a large e-folding scale height ratio H/R of about 0.5. The mass of the entire disk estimated from the column density is discussed depending on the assumed distance and the dust model and ranges between 0.02 and 5 $M_\odot$. We conclude that unless a star is located close to the disk in the foreground, scattered light will have little influence on the mass determination. We present a Spitzer image taken at $\lambda = 7.8$ μm with the disk seen in emission and identify polycyclic aromatic hydrocarbon (PAH) emission on the disk surface excited by the nearby massive stars as a possible source. Our 3D radiative transfer calculations for the scattered light image of the central source through an edge-on disk indicate that the elliptical shape seen in the NACO image does not require the assumption of a binary system and that it is consistent with a single object. We derive stellar main sequence masses of several $M_\odot$, 50 $M_\odot$, or 10 $M_\odot$, depending on our assumptions that the extinction of the stellar flux is dominated (i) by the outer disk, (ii) by an inner disk comparable to the disks around intermediate-mass stars, or (iii) by an inner disk with dominating hot dust emission. We find that even for a star-disk mass ratio of 1, only the outer parts of the circumstellar disk may be influenced by self-gravity effects due to the large e-folding scale height ratio.

Key words. radiative transfer – accretion, accretion disks – stars: formation – stars: circumstellar matter

1. Introduction

Our understanding of the star formation process in general is very limited, and this is especially true for the formation of massive stars. While they are easily observable once they have started their dominating influence on the parental star-forming regions (SFRs), the initial processes of star formation are hidden behind the dense material enshrouding the young objects. Several other aspects hinder an observational exploration of the early evolution of massive stars: (i) the time window for observing a massive star during its formation phase of a few 10^5 years is short compared to less massive stars; (ii) the number of massive stars is below 1% of the total number of stars; (iii) massive stars often form close to each other inside dense clusters, making it difficult to isolate one object for further investigation; (iv) radiation pressure and winds reshape high-mass SFRs into complex environments with substantial potential for confusion of sources and structures; and (v) the closest low-mass SFRs are at distances of 140 pc, while the nearby massive SFRs with the exception of Orion are more than 1 kpc away, making coarse resolution an important observational issue.

While observations show that young low- and intermediate-mass stars are surrounded by a circumstellar disk that are often actively accreting matter from it, only a few candidates for such

⋆ Based on observations collected at the European Southern Observatory, Chile ESO No. 270.C-5040.

a circumstellar disk around a massive star are known (Gehrz et al. 1982; Marti et al. 1993; Greenhill et al. 1998; Shepherd et al. 2001; Hofner et al. 2001; Sandell et al. 2003). It was argued by Wolfire & Cassinelli (1987) that the strong radiation pressure of the young massive star might hinder spherical symmetric accretion onto the star to reach high masses of several 10 solar masses. Yorke & Sonnhalter (2002) have performed 2D hydrodynamical grid simulations of a collapsing cloud including non-gray radiative transfer with flux-limited diffusion. They found that for initial cloud masses of 120 $M_\odot$, a massive disk can form around the central star with final masses of the star reaching about 43 $M_\odot$. Alternatively, Bonnell & Bate (2002) proposed that merging of intermediate-mass stars may lead to the formation of massive stars. However, it needs to be verified that the probability of stellar collisions is high enough in all massive star formation regions to account for the observed population (for a comparison of both scenarios see, e.g., Bally & Zinnecker 2005).

In the following, we will use the term *massive disk* for any flattened structure around a single or multiple protostars or stars that has a sufficient mass to build up a massive star or that is the remnant of such a process. Evidence for a massive disk candidate seen in silhouette against the bright HII light in the massive SFR M 17 was published by Chini et al. (2004, hereafter Cea04). They have interpreted the two triangular shaped dust lanes seen in the NAOS/CONICA 2.2 μm image as an almost edge-on accretion disk surrounded by a flattened envelope. Assuming a distance of $D = 2.2$ kpc, the total extent of the structure was determined to be 20 000 AU. From the ^{13}CO Plateau de Bure observations, they derived a total mass of the silhouette structure of 110 $M_\odot$.

Among the many aspects of the object, two features are of major importance: (i) silhouette structures have the substantial advantage that for a known intensity of the background radiation, the column density distribution can be determined with the resolution of the corresponding image. On the contrary, for images where the gas structure is seen also in emission, both absorption and emission have to be taken into account, which allows us to deduce only mixed density and temperature information without elaborate theoretical modeling; (ii) the extent of the structure interpreted as circumstellar disk would exceed that of commonly observed disks around low-mass stars by a factor larger than 10.

Consistent with the picture of a central object surrounded by a flattened structure, an hourglass-shaped nebula perpendicular to the hypothetical disk midplane is visible in images ranging from 0.4 to 2.2 μm. The emission lines in the spectrum showed characteristic profiles interpreted as accretion signatures, similar to the signatures seen for young low-mass stars. Assuming that the central object is a main-sequence star, its mass was derived from the absolute infrared brightness and is about 20 $M_\odot$. The position-velocity diagram of the ^{13}CO data was compared to a rotation curve of a thin edge-on disk rotating rigidly in the inner parts and with Keplerian motion in the outer parts assuming a stellar mass of 15 $M_\odot$.

The silhouette pattern was re-analyzed in Sako et al. (2005, Sea05) making use of their Subaru IR-images as well as ^{13}CO Nobeyama millimeter array data. These authors have named the object M 17 SO1. From the absence of a compact HII region and a non-detection of the central source in the 12.8 μm COMICS image, and assuming a distance of 1.5 kpc, they constrained the mass of the central object to be <8 $M_\odot$. The total mass of the inner and outer envelope hosting the silhouette structure was estimated from the NIR column density to be 0.09 $M_\odot$, and 4 $M_\odot$ for the entire local molecular cloud hosting the silhouette structure, respectively (a factor of 2 higher assuming 2.2 kpc instead of 1.5 kpc distance). In turn, an estimate of the total gas mass of the cloud derived from the ^{13}CO data lead to about 9 $M_\odot$. The spatial distribution of the envelope was discussed in terms of a simple iso-thermal model assuming dynamical equilibrium of the thermal pressure gradient with the vertical component of the stellar gravity. It was pointed out in Sea05 that four arms indicate the location of shells being swept up by the bipolar outflow of the central source, and that they are detached from the envelope. This would imply a scenario in which the shape of the silhouette structure is not formed by an evacuation of an originally more spherical envelope.

Given the importance of finding a circumstellar disk around a young stellar object with the potential to reach a mass beyond 10 $M_\odot$, the apparent diversity in the results in Cea04 and Sea05, and the advantageous silhouette situation, we give a more detailed analysis of the presented data.

An important parameter for the determination of the size and the mass of both the disk and the central object is the distance to the SFR M 17. A new kinematic determination presented in Russeil (2003) estimated the distance to be 2.4 kpc. Earlier studies like Hanson et al. (1997) were based on a small sample of O-stars and their luminosity which were not accurately known. As our own Hertzsprung-Russell diagram with several thousand of stars also indicates a value greater than 2.2 kpc, we will use this value.

In this paper, we apply a simple circumstellar disk model to constrain the density distribution of the massive disk candidate. In Sect. 2, we determine a map for the optical depth distribution in the region of the silhouette structure and discuss its morphology. We also give an estimate of the total mass in the silhouette structure assuming dust particles typical of the interstellar medium. A circumstellar density distribution is fitted to the column density map in Sect. 3. We discuss the influence of scattered light using continuum radiative transfer calculations and different dust properties. The mass in the disk as a function of the radius is given for the different dust models. New Spitzer data showing an emission feature at the disk location at 7.8 μm are presented. Moreover, using the derived disk parameters, we discuss its stability against gravitational instabilities for a star-to-disk mass ratio of 1. In Sect. 4, we derive constraints for the mass of the central object using the flux values or limits at different wavelengths and various assumptions about the star, the dust grain size, and emission from the hot dust in the inner parts. The findings are summarized and discussed in Sect. 5.

2. Optical depth distribution of the silhouette structure in the NACO image at 2.2 μm

2.1. First estimate of the total mass in the silhouette structure

The optical depth along the line of sight (x-axis, Cartesian coordinates) is

$$\tau^\lambda_{y,z} = \int_{-\infty}^{+\infty} \sigma^\lambda_{\rm ext}\, n(x,y,z)\, {\rm d}x = \sigma^\lambda_{\rm ext}\, N_{y,z} \qquad (1)$$

with the extinction cross section $\sigma^\lambda_{\rm ext}$, the dust particle number density n, and the dust particle column number density $N_{y,z}$. For clarity, we will suppress the wavelength-label and refer to $\lambda = 2.2$ μm. In this work, we will assume that the dust particles are equal throughout the disk, and neglect effects of coagulation, sedimentation, or size-dependent radiation pressure effects. We defer discussion of this aspect to a forthcoming paper.

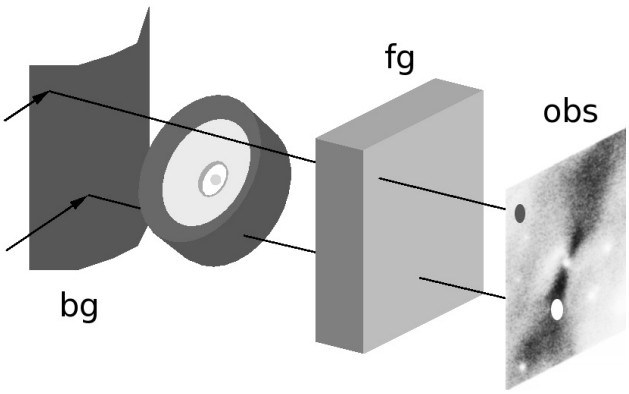

Fig. 1. Sketch of the different layers contributing to the observed optical depth. The black spot in the image indicates the location where the observed background is determined, the bright spot, where the observed intensity is analyzed to derive the observed optical depth due to the extinction by the disk material.

Figure 1 shows a sketch illustrating our notation of the different layers entering the optical depth analysis in this paper. Radiation is scattered in the background towards the disk and the observer. We assume here that this radiation is constant over the area of the image and has the flux value of $F_{\rm bg} = 3.6$ mJy/pixel derived from a representative area well outside the silhouette pattern.

A first estimate of the order of magnitude of the optical depth can be found from the image calculating

$$\tau_{y,z}^{\rm obs} = -\ln\left(\frac{F_{y,z}}{F_{\rm bg}}\right). \quad (2)$$

We consider homogenous silicate spheres of size $a = 0.1$ μm as dust particles, with optical properties taken from Draine & Lee (1984). Each dust particle has a mass of

$$m_{\rm dp} = \rho_{\rm dp}\frac{4}{3}\pi a^3 \quad (3)$$

for an inner dust particle density of $\rho_{\rm dp} = 3 \times 10^3$ kg m^{-3}. The dust particle column number density per pixel is $N_{\rm pxl} = N_{y,z}\, A_{\rm pxl}$, where $A_{\rm pxl} = (60\ {\rm AU})^2$ is the pixel area of the NACO image for a distance of $D = 2.2$ kpc. Using a gas to dust mass ratio $W = 100$ (e.g. Vuong et al. 2003), we obtain an estimate of the mass in the silhouette area ranging up to the radius of 9000 AU of

$$M_{\rm da} = -\frac{W\, m_{\rm dp}\, A_{\rm pxl}}{\sigma_{\rm ext}} \sum_{y,z} \ln\left(\frac{F_{y,z}}{F_{\rm bg}}\right) = 5.1\ M_\odot. \quad (4)$$

This value has large error bars, as the dust properties are uncertain, the background might vary, some rest foreground material might be present, the distance is uncertain, and the influence of scattering is neglected.

2.2. Range and distribution of optical depths

The optical depth defined in (2) ranges roughly from 0.7 to 2.4 for the "disk" area. Figure 2 shows the optical depth of the inner 100 × 100 pixels of the image, corresponding to 6000 AU × 6000 AU for a distance of $D = 2.2$ kpc (shaded surface). Due to the pixel noise in the NACO image, we have smoothed the image to improve the visibility of the structure.

To reveal the symmetry in the silhouette pattern, we have rotated in Figs. 3 and 4 the optical depth map derived from the image such that the connecting line of the maxima and the central

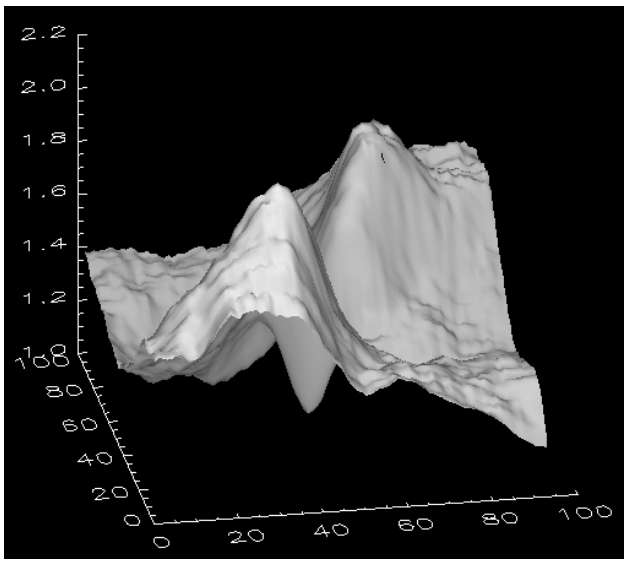

Fig. 2. Shaded surface representation of the optical depth of the central part of the smoothed image (inner 6000 AU × 6000 AU).

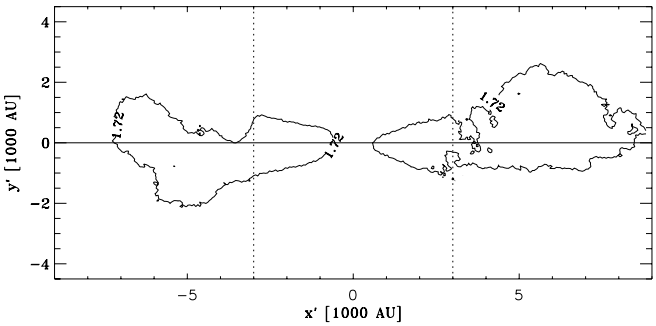

Fig. 3. Symmetry in the optical depth derived from the NACO image at 2.2 μm (contour line for $\tau = 1.72$). The solid line is the cut of the disk midplane and the sky plane. The dashed lines indicate the approximate border of the change from axis-symmetry to point-symmetry.

emission pattern (the midplane, if interpreted as edge-on disk-like structure) is horizontally oriented (with the rotated sky plane coordinates x' and y'). The $\tau = 1.72$ contour line in Fig. 3 resembles the outer shape of the disk. The dashed lines indicate the approximate location of the limits between axis-symmetry and point-symmetry. The optical depth in the northern (southern) part of the structure is displayed in the upper (lower) part of Fig. 4 as a contour plot. The southern part has been reversed vertically. Although the underlying NACO map is noisy and there are confusions from nearby stars, two major symmetries are seen: (i) the inner part with optical depths $\tau > 1.4$ out to distances of 3000 AU shows indications of mirror symmetry with respect to the $x' = 0$-axis; (ii) the twist of the pattern in the outer regions at $x' > 3000$ AU with $\tau > 1.4$ indicates a level of point-symmetry with respect to the center. The point-symmetry in the regions around 8000 AU is probably stronger than depicted in the contour plots as a star disturbs the southern map at $(x', y') =$ (7800 AU, −1000 AU).

Such a symmetry is unlikely if the structure is explained by a filament seen in front of a stellar object. The outer point symmetry might be interpreted as being produced by an external large scale motion or radiation pressure effect, but the strong inner axial symmetry points towards a central domination.

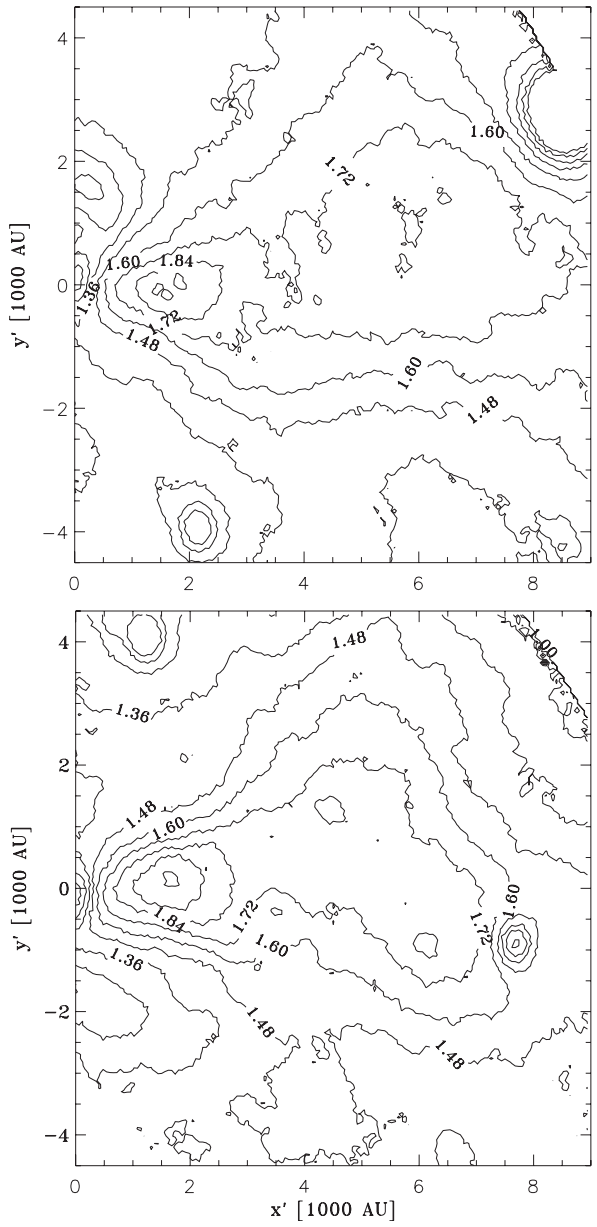

Fig. 4. Symmetry in the optical depth derived from the NACO image at 2.2 μm. The optical depth map has been divided along a line vertically to the solid line in Fig. 3. The lower panel has been reversed vertically for better visibility of point-symmetry in the outer parts of the silhouette pattern.

In the following, we want to examine wether the optical depth distribution of the silhouette structure is in agreement with a circumstellar disklike structure and to derive some of its physical properties.

3. Circumstellar disk model

3.1. Spatial distribution of the optical depth at 2.2 μm

With the use of high angular resolution imaging techniques in the optical, infrared, and millimeter bands, a number of resolved disks surrounding pre-main sequence stars have been identified (see, e.g., Hartmann et al. 1998). Interpreting these disks as accretion disks, most models assume that the central low- or intermediate-mass star has been formed by accretion through the disk (see, e.g., Cassen & Moosman 1981). However, circumstellar disks around more massive stars might have a density and temperature structure that significantly deviates from the low-mass analogs. There are indications of a thermally expanded inner rim of the disk around intermediate-mass Herbig AeBe stars that causes complex shadowing effects and is visible in the SED. The strong radiative heating from the central star can enforce disk flaring or can have a kinematic effect on the outer disk layer (Dullemond & Dominik 2004). The massive disk may undergo instabilities due to self-gravitation and also external radiation and winds from nearby massive stars may reshape and heat the disk. In view of these many unknown processes in addition to the complex accretion disk physics of low-mass stars, we will assume a parameterized density distribution similar to the circumstellar disk models for low-mass stars but with enough freedom to adapt to the changed physical situation (see, e.g., Pascucci et al. 2004). Note that we are not intending to fit only the spectral energy distribution (SED) (this would be ambiguous, see Thamm et al. 1994), but we perform a multi-parameter fit of the NACO 2.2 μm image with about 8000 pixels. The diffraction limit of NACO/VLT of 0.″056 (*FWHM*) at 2.2 μm is larger than the pixel resolution of 0.″027/pixel, so that the amount of information is lowered by about a factor of 3 as the information in each pixel is not independent of the neighboring pixels. Nevertheless, the number of data values is two orders of magnitude larger than the number of fit parameters.

For the density distribution of the dust particles, a number density distribution of the form

$$n(x, y, z) = n_0 \left(\frac{r}{r_0}\right)^{-\alpha} \exp\left[-\left(\frac{z}{rh}\right)^2\right] \quad (5)$$

is assumed with the midplane radius $r = \sqrt{x^2 + y^2}$, the number density normalization n_0, the inner radius r_0, the outer radius of about 10 000 AU, the radial powerlaw exponent α, and the e-folding scale height ratio $h = H/R$ (H is the z-value for which the density has dropped by $1/e$ for a given radius). By varying n_0, α, h, the inclination of the disk i, the angle δ between the cut-line of disk and sky plane and the x-axis, and the position of the star in the cut-image (x_t, y_t), we can mask and model the silhouette pattern within the radial range 800 AU to 4500 AU.

The inner part of the disk close to the central object is not well-suited for a silhouette modeling, as the absorption of the assumed background radiation can be confused with the central emission, possible disk emission, and scattered radiation. We therefore exclude the inner 1000 AU from our modeling although the disk likely will extend into this part, as the dust particles can be expected to exist up to a sublimation temperature of about $T_s = 1500$ K at the radius r_s. If we consider optically thin emission for $r < r_s$ at all wavelengths where substantial stellar energy is transported, and a complete conversion of the energy in a small layer around r_s, we find $r_s = R_*(T_*/T_s)^2$. Here, we also assumed that there are no additional heating sources like anomalous viscosity, magnetic reconnection, or losses due to scattering. For a stellar mass of 15 $M_\odot$, the sublimation radius is about 20 AU, which is well within the inner pixel. However, the evolutionary state of the central object(s) is unknown, and the radius and effective surface temperature might be different from that of a main-sequence star. It seems likely that the gaseous part of the disk extends even beyond this point, as accretion signatures have been found by Cea04 in the reflected light of the hourglass nebula.

The image and the masked area are shown in the top left and right panels of Fig. 5, respectively.

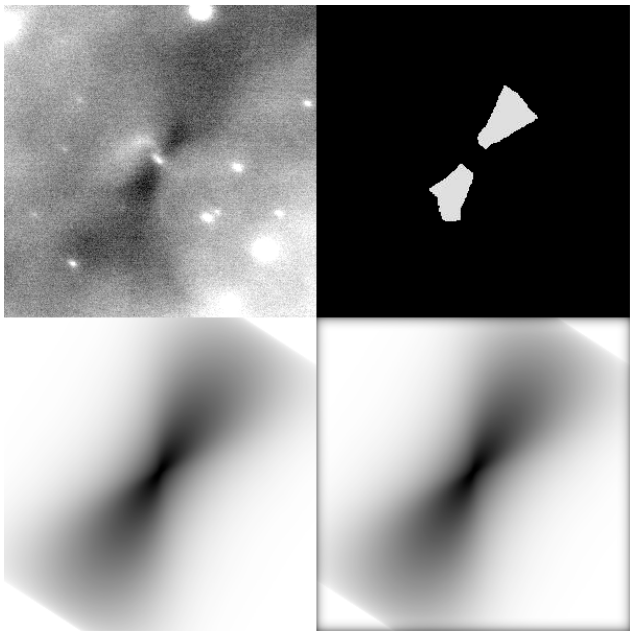

Fig. 5. Original 2.2 μm NACO image, mask for the column density fit, best fit theoretical absorption image, and the same image convolved with the NACO point spread function, respectively. The image width is 18 000 AU.

Table 1. Table of parameters obtained by the fit of the absorption dominated regions.

Parameter	Label	Value
density normalization	n_0	319 m^{-3}
radial index	α	1.13
disk inclination	i	12.3°
e-folding scale height ratio	h	0.476
sky orientation	δ	56.5°

Choosing a pixel with the intensity $I_{\rm bg}$ that is located in a flat, less absorbed background area, and assuming that the background does not differ much from this mean background value, we can define the intensity in the image to be of the form

$$I^{\rm obs}(y,z) = I^{\rm obs}_{\rm bg} \exp\left[-\tau^{\rm obs}(y,z)\right]. \quad (6)$$

The error introduced by assuming an inaccurate background intensity is most likely larger than the 10% level of noise in the NACO image. Having calculated the intensity for all marked pixels, we can vary the free parameters to find a density structure that reproduces the absorption dominated parts of the image. As a minimizing algorithm for the χ^2-fit, we used the Metropolis algorithm *simulated annealing* (for details see, e.g., Thamm et al. 1994). In Fig. 5, the lower pictures give the theoretical best-fit image without (left) and with (right) convolution with the point spread function (PSF) of the telescope. (The fit has been performed including PSF-convolution). The resulting parameters are listed in Table 1. A two triangles-appearance of the disk as in the original image appears to be possible. The disk inclination and the sky orientation are confined to a 10% deviation by the fit, while the other parameter being related to the column density, allow larger variations.

Note that while for the masked area entering the fit, only the inner part of the disk up to about 4500 AU was chosen, the resulting theoretical images also resemble the mean absorption in the outer parts well. The only difference is the warp in the structure, best visible in Fig. 3, that causes the image to be point-symmetric rather than axisymmetric, as in the inner parts.

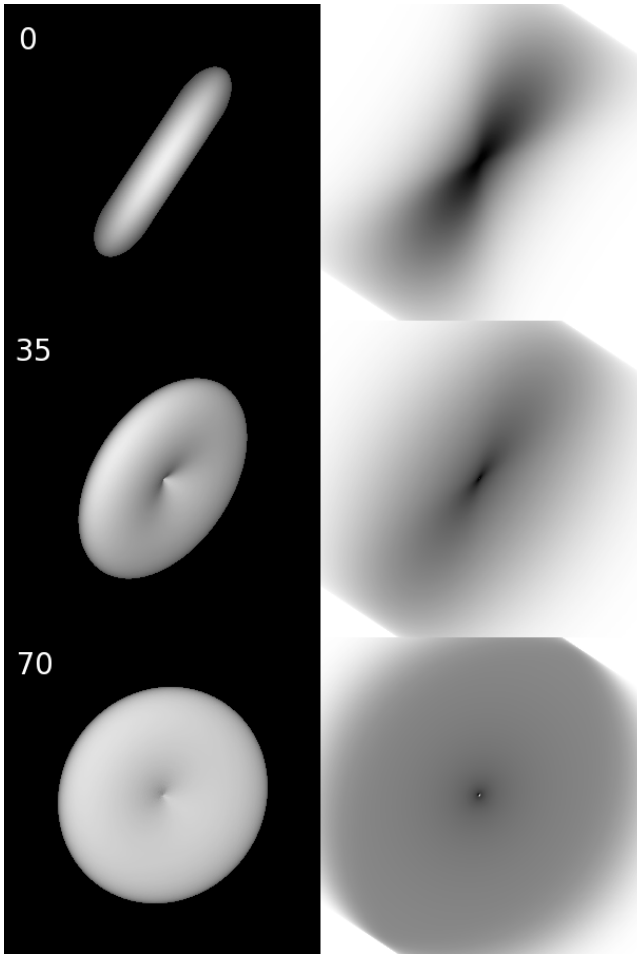

Fig. 6. Theoretical absorption image of the circumstellar disk using the optimized fit parameters and varying the inclination angle against the edge-on case. The *left panel* shows an isodensity surface of the disk distribution (the inclination angle against the edge-on case is given in degrees). The *right panel* shows the corresponding 2.2 μm absorption image.

3.2. Influence of scattered light on the optical depth through the circumstellar disk

In this section, we investigate how scattered light can influence the determination of the optical depth within the disk. For the derivation of the optical depth within the disk from the observed optical depth, we refer to Fig. 1. Radiation is scattered in the background towards the disk and the observer. We assume here that this radiation is constant over the area of the image and has the intensity $I_{\rm bg}$.

The intensity of the radiation passing the outer borders of the disk will not decrease due to absorption and a small component of scattered light $\mathit{I}_{\rm bg}$ will be added. After leaving the foreground layer with the optical depth $\tau_{\rm fg}$ to propagate towards the observer, the intensity has the value

$$I^{\rm obs}_{\rm bg} = \left(I_{\rm bg} + \mathit{I}_{\rm bg}\right) \exp\left[-\tau_{\rm fg}\right]. \quad (7)$$

Radiation in the same direction additionally entering the disk will experience absorption described by the optical depth $\tau(y,z)$, so that the intensity is $I_{\rm bg} \exp\left[-\tau(y,z)\right]$. When leaving the disk,

radiation will be scattered into the considered direction with the intensity $\mathcal{I}(y,z)$. After crossing the foreground layer, the observed intensity of radiation through the disk is

$$I^{\rm obs}(y,z) = I_{\rm bg}\exp\left[-\tau(y,z)-\tau_{\rm fg}\right] + \mathcal{I}(y,z)\exp\left[-\tau_{\rm fg}\right]. \quad (8)$$

In the last section, we derived the observed optical depth using (6). Inserting (7) and (8), the foreground absorption cancels out and the real optical depth is

$$\tau(y,z) = -\ln\left\{\left(1+\frac{\mathcal{I}_{\rm bg}}{I_{\rm bg}}\right)\exp\left[-\tau^{\rm obs}(y,z)\right] - \frac{\mathcal{I}(y,z)}{I_{\rm bg}}\right\}. \quad (9)$$

For small observed optical depth $\tau^{\rm obs}(y,z) \ll 1$, we obtain

$$\tau(y,z) \approx \tau^{\rm obs}(y,z)\left(1+\frac{\mathcal{I}_{\rm bg}}{I_{\rm bg}}\right) + \frac{\mathcal{I}(y,z)-\mathcal{I}_{\rm bg}}{I_{\rm bg}}. \quad (10)$$

If no absorption is observed, the real optical depth will have the finite value $\mathcal{I}(y,z) - \mathcal{I}_{\rm bg}/I_{\rm bg}$ to absorb the scattered light contribution. Aside from this offset, $\tau(y,z)$ will rise linearly with $\tau^{\rm obs}(y,z)$ with a gradient that is expected to be close to 1 for $\lambda = 2.2\,\mu$m, where absorption is about a factor of 5 stronger than scattering for typical interstellar medium dust particles.

For larger observed optical depth, the scattering can cause substantial differences between $\tau(y,z)$ and $\tau^{\rm obs}(y,z)$. In this case, the observed intensity is low compared to the observed background intensity. As the scattered part of the radiation is added after the absorption within the disk, it builds up a large fraction of the observed intensity, leaving just a small fraction for the radiation in the disk. This means that the real optical depth must be very large. In the extreme case of

$$\tau^{\rm obs}(y,z) = \ln\left(\frac{I_{\rm bg}+\mathcal{I}_{\rm bg}}{\mathcal{I}(y,z)}\right), \quad (11)$$

the real optical depth must be infinitely large to satisfy (9), and $\tau(y,z)$ is not defined for larger $\tau^{\rm obs}(y,z)$.

To estimate the order of magnitude effect of scattering and the distribution of scattered light in the image plane, we have performed a 3D radiative transfer calculation using the code described in Steinacker et al. (2003; updates described in Steinacker et al. 2004, 2005). The density distribution (5) was used with the parameters obtained in the image fit. We performed separate calculations using small grains with $a = 0.1\,\mu$m typical of the interstellar medium and larger grains with $a = 1\,\mu$m to account for a possible grain growth or radiative pressure effects on dust grains. The scattering properties of dust grains have been computed by the standard Mie theory (Mie 1908), using the modified code of Barber & Hill (1990). The dust particles are assumed to be homogeneous spheres of a uniform size (radii a between 0.02 μm and 200 μm) made of pure astrosilicate (Draine & Lee 1984; Draine 1985). The corresponding phase functions have been calculated with an angular step size of 1°, using logarithmically-spaced size and wavelength grids of 100 points. The accuracy of the computed phase functions is better than 0.01%.

The computational domain of $(20\,000\ {\rm AU})^3$ was discretized in 8×10^6 grid cells. For the direction discretization, an optimized node distribution obtained by simulated annealing proposed in Steinacker et al. (1996) was used with $N_{\rm d} = 200$ nodes. This corresponds to an angular resolution in direction of about 14°. The outer boundary condition for the radiation field is very complex with several nearby high-mass stars, as well as other stars and a complex filamentary structure absorbing and scattering the radiation. Lacking the knowledge of the 3D structure in the M 17 region, the outer radiation field cannot be given correctly. To estimate the effect of scattered light on the optical depth determination, we have imposed an isotropic radiation field. The scattered light of the central object was not included, as it will appear mainly in the polar regions above the disk and therefore not influence the optical depth determination for the almost edge-on disk view discussed here.

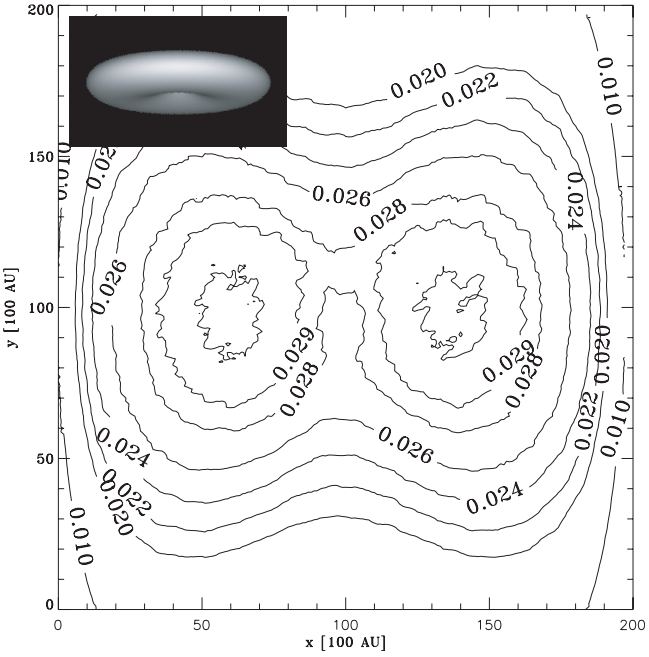

Fig. 7. Calculated image of the scattered radiation for homogenous external illumination of the circumstellar disk. The inclination of the disk is visualized by the left upper inlet showing an isodensity surface of the density. The dust is assumed to be homogenous spherical silicate grains of size 0.1 μm. The contours are labeled with the intensity value normalized to the background intensity.

The scattering of the 0.1 μm-sized silicate dust particles can be treated by the Rayleigh limit approximation since they are much smaller than the wavelength of incident radiation $\lambda = 2.2\,\mu$m, leading to a scattering phase function that is peaked forward by a factor of 2 more compared to the scattering in the perpendicular direction (see Steinacker et al. 2003, for details).

Figure 7 shows the distribution of scattered radiation for homogenous external illumination at 2.2 μm of the circumstellar disk. The inclination of the disk is indicated in the upper left inset showing an isodensity surface. The labels give the intensity value normalized to the background intensity. The noise in the contour lines is due to the finite spatial and angular resolution. Two maxima arise symmetrically at distances of about 3800 AU from the center. This is because the optical depth is low enough that the radiation can penetrate the disk substantially before being scattered, so that the scattering pattern is not surface-dominated but has a column density-dominated double-peak appearance. Therefore, scattering of isotropic radiation will be strongest in the central parts that have been used for the optical depth modeling and could therefore influence the derived optical depth value. From Fig. 7, the ratio of scattered to background intensity is $\mathcal{I}(y,z)/I_{\rm bg} < 3.1 \times 10^{-2}$. In the area far from the disk structure where the background intensity was chosen, the ratio is about $\mathcal{I}_{\rm bg}/I_{\rm bg} \approx 10^{-2}$. We can determine the real optical depth $\tau(y,z)$ for each pixel of the image using (9). In Fig. 8, the difference $\tau(y,z) - \tau^{\rm obs}(y,z)$ is plotted for the northern part of

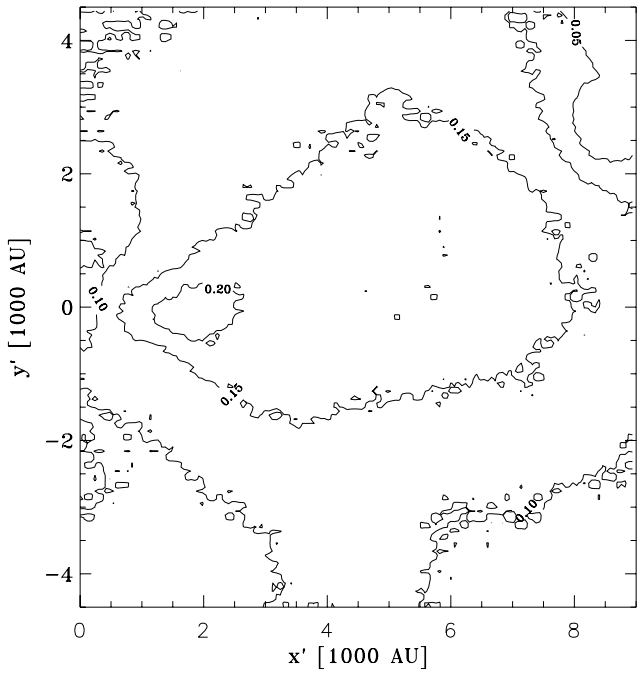

Fig. 8. Difference between the observed optical depth and the real optical depth taking into account scattered light for the northern half of the circumstellar disk. The notation is the same as in Fig. 4. The contour levels refer to 0.05, 0.10, 0.15, and 0.20.

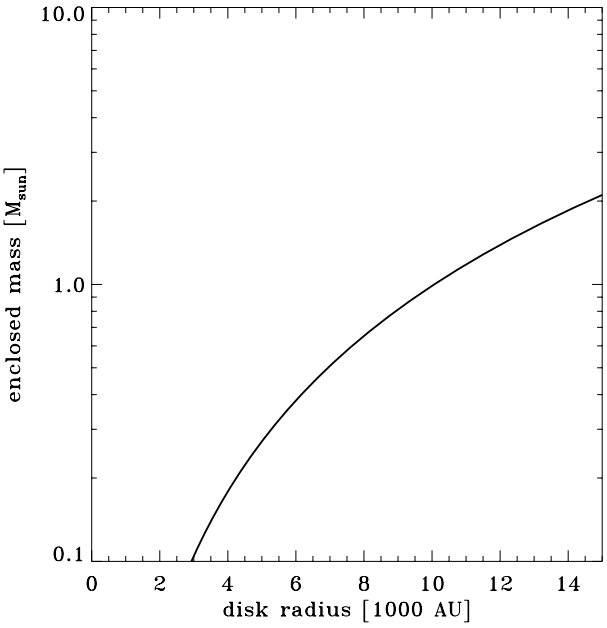

Fig. 9. Enclosed mass of a circumstellar disk as a function of the outer radius R assuming silicate spheres of size 0.1 μm.

the circumstellar disk (see Fig. 4 for the notation). As it can be read from the contour labels, $\tau(y,z) < \tau^{\rm obs}(y,z)+0.21$. Assuming small particles, scattering will therefore not influence the optical depth determination considerably.

It might be argued that due to grain growth or selection effects by radiative pressure, larger particles of size $a = 1$ μm might dominate the size distribution in the disk. As the optical depth is fixed from the observation, the main change for larger particles is the strong forward scattering. The probability that radiation is scattered into the line of sight is therefore reduced except for the radiation already being close to the line of sight. But this radiation either crosses the disk atmosphere or is absorbed while crossing the disk. The amount of scattered light in the masked disk area used for the fit is therefore strongest for the small particles. We will take the modification of the optical depth due to scattered light into account when estimating the disk mass in Sect. 3.3.

3.3. Mass of the circumstellar disk

Using the parameters from the simulated annealing fit of the image, we can determine the mass of the disk up to a radius R by integrating over the circumstellar disk distribution. The total number of dust particles is

$$N_{\rm dp} = \int_0^{2\pi} {\rm d}\phi \int_{r_0}^{R} r\,{\rm d}r \int_{-\infty}^{+\infty} {\rm d}z\, n(r,\phi,z) \tag{12}$$

$$= 2\pi^{3/2} n_0 h r_0^{\alpha} \left| \frac{1}{3-\alpha} r^{3-\alpha} \right|_{r_0}^{R}, \tag{13}$$

where we have used $\int_0^{+\infty} {\rm d}t \exp\left[-A^2t^2\right] = \sqrt{\pi}/2A$ and obtain for the cumulative disk mass

$$M_{\rm disk}(R) = \frac{2}{3-\alpha}\pi^{3/2} n_0 h W m_{\rm dp} r_0^3 \left[\left(\frac{R}{r_0}\right)^{3-\alpha} - 1\right]. \tag{14}$$

The normalization of the number density n_0 can be estimated from the maximal optical depth found in the image of about 2.4, including the maximal deviation due to scattered light of about 0.21 derived in Sect. 3.2. The optical depth along a line of sight through the central region having an angle of i to the plane of the disk and the x-axis is ($y = 0$)

$$\tau_{\rm max} = 2\sigma_{\rm ext}\, n_0 \int_{r_0}^{\infty} {\rm d}x \left(\frac{x}{r_0}\right)^{-\alpha} \exp\left[-\left(\frac{x\tan i}{xh}\right)^2\right] \tag{15}$$

$$= \frac{2\sigma_{\rm ext}\, n_0 r_0}{\alpha - 1} \exp\left[-\frac{\tan^2 i}{h^2}\right] \tag{16}$$

for $\alpha > 1$. Solving (15) with respect to n_0 and inserting into (12), we find

$$M_{\rm disk}(R) = \frac{4}{3}\pi^{3/2}\frac{\alpha-1}{3-\alpha}\tau_{\rm max} h \rho_{\rm dp} W \frac{a}{Q_{\rm ext}} r_0^2 \times \left[\left(\frac{R}{r_0}\right)^{3-\alpha} - 1\right] \exp\left[\frac{\tan^2 i}{h^2}\right] \tag{17}$$

with the extinction coefficient $Q_{\rm ext}$ defined by $\sigma_{\rm ext} = \pi a^2 Q_{\rm ext}$.

From Fig. 9 displaying the relation for silicate spheres of size 0.1 μm, we find that the disk mass out to 8000 AU is about 0.6 $M_\odot$. As the warped outer parts with point symmetry seems to have the same area extinction as the axisymmetric outer parts of the theoretical image, in first approximation, the warping can be interpreted as a translation. This leads to a rough estimate of the mass in the outer part of several solar masses.

The error in the mass determination from applying the circumstellar disk model is hard to quantify. We performed fits

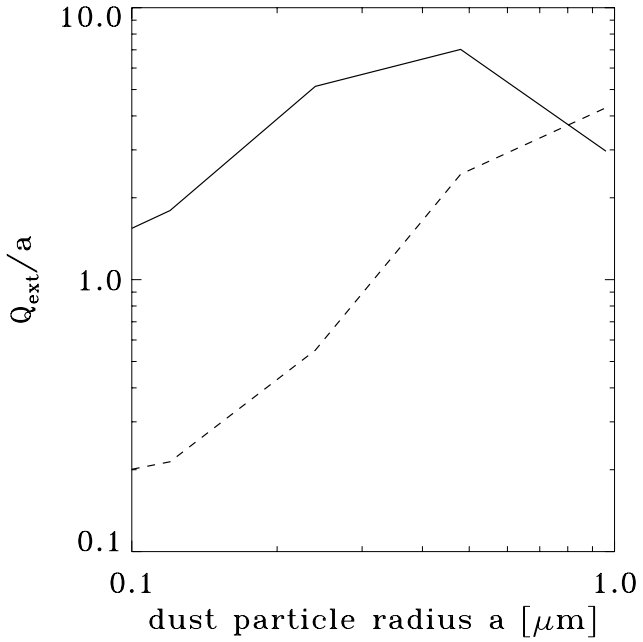

Fig. 10. Ratio of the extinction coefficient and the dust particle size as a function of the particle size. The solid line refers to carbon spheres and the dashed line to silicate sphere.

assuming two radial powerlaws in density and obtained similar results. We will therefore assume here that the error from a possibly incorrect modeling of the density distribution does not exceed a factor of 2.

Another effect altering the disk mass would be an inhomogeneous background illumination. Investigating the neighborhood of the silhouette, such gradients are visible. We have chosen different regions close to the disk, masked the stars, averaged the flux, and found deviations of about a factor of 3. As foreground star halos or filaments can further alter the appearant background, we will use a factor of 4 as a possible error in the background leading to an uncertainty in the optical depth of about ±1.4.

The optical properties of the dust particles are far from being known. They enter (17) in the form of the ratio $a/Q_{\rm ext}$ and the inner dust particle density $\rho_{\rm dp}$. Figure 10 shows the inverse value $Q_{\rm ext}/a$ as a function of the grain size for carbon (solid line) and astro-silicate (dashed line) spheres, respectively, after Draine & Lee (1984). It is likely that grains will have a size distribution ranging from interstellar grain sizes of 0.1 μm to larger grains of about 1 μm, likely produced by coagulation. For all these grains, the ratio $a/Q_{\rm ext}$ would be smaller and hence smaller disk masses would be derived using (17). The same is true changing the chemical composition of the grains to contain a larger fraction of carbon. As seen in Fig. 10, for a C grain, $Q_{\rm ext}/a$ is a factor of 8 larger than for Si which cannot be compensated for by the lower inner density (factor of 2). Given the other uncertainties and the limited information about the physical properties in the disk, we have not performed more detailed modeling of the dust properties including coagulation, ice mantels, porosity, etc. Thus, we estimate the change in the mass due to various assumed dust properties from about a factor of 3 larger to a factor of 8 smaller than the presented silicate spheres with a uniform size of 0.1 μm.

Finally, the inner radius of the disk is unresolved in the image and was estimated in Sect. 3.1 to be of the order of 20 AU for a 15 $M_\odot$ star. From (17), we find that for outer radii of around R = 10 000 AU, the r_0-dependency almost cancels out, as the radial powerlaw index determined from the image fit is close to 1 (α = 1.13). We conclude that within this model, the inner radius has little influence on the estimated disk mass. Note that we assume here that the density distribution, found from modeling the outer parts of the disk, is valid for the inner parts as well (see also Sect. 4.3).

Thus, we find that the mass of the disk up to a radius of 8000 AU is between 0.02 and 5 $M_\odot$. Due to the large extent of the structure and the moderate optical depth in the NIR, the temperatures in the disk structure might not be lower than a few 10 K so that coagulation is largely depressed, leaving small dust particles similar to the ones observed in the interstellar medium to be the dominant dust species in the disk.

The model is therefore consistent with the interpretation of the silhouette object as a massive circumstellar disk with the large extent of about 10 000 AU in radius.

We note that the mass estimates derived in Cea04 from the ^{13}CO 1–0 line data are at least a factor of 8 higher either due to an approximative mass conversion relation or due to contamination by foreground emitting gas.

3.4. The circumstellar disk seen in the Spitzer image at 7.8 μm

The region containing the massive disk candidate in M 17 has been mapped in the framework of the Spitzer GLIMPSE survey of the galactic plane carried out with the IRAC instrument (Werner et al. 2004; Fazio et al. 2004). The disk is detected at 7.8 μm in absorption with a central extended hole or emission feature (see Fig. 11). The upper limits are the 3-sigma level of the rms noise at the locus of the disk. As this band includes the strongest polycyclic aromatic hydrocarbon (PAH) emission lines outside a possible silicate feature at 10 μm, it is likely that the both the background emission and the extended emission from disk arises from PAHs excited by the ambient UV radiation field. This is supported by the fact that the structure is not detected in emission in the other Spitzer filter. The morphology of the radiation field is poorly known, and to treat PAHs means a substantially increased numerical effort compared to continuum emission. Furthermore, additional parameters would have to be introduced that cannot be constrained from other information sources. Hence, we refrain from modeling the image at 7.8 μm with the density structure derived in this section and will perform further investigations in a forthcoming paper.

3.5. Gravitational stability of the circumstellar disk

With up to 5 $M_\odot$ of gas and dust disk rotating around a central object that possibly has comparable or higher mass, the role played by self-gravity and even the actual gravitational stability of the material in these outer regions are important issues. When disks are seen face-on, instabilities are usually easy to detect as these take the form of non-axisymmetric patterns (rings, arms, or bars). For systems seen edge-on like the massive disk candidate discussed here, the evidence is less straightforward to verify (a significant disk shrinking or anti-flaring could be present; see Huré 2000).

A qualitative analysis of the M 17 silhouette supports the possible occurrence of self-gravity in the outer parts. The e-folding scale height ratio of ~0.5 is high compared to scale heights usually observed for older accretion disks around low-mass stars. The kinetic temperature is probably too low to

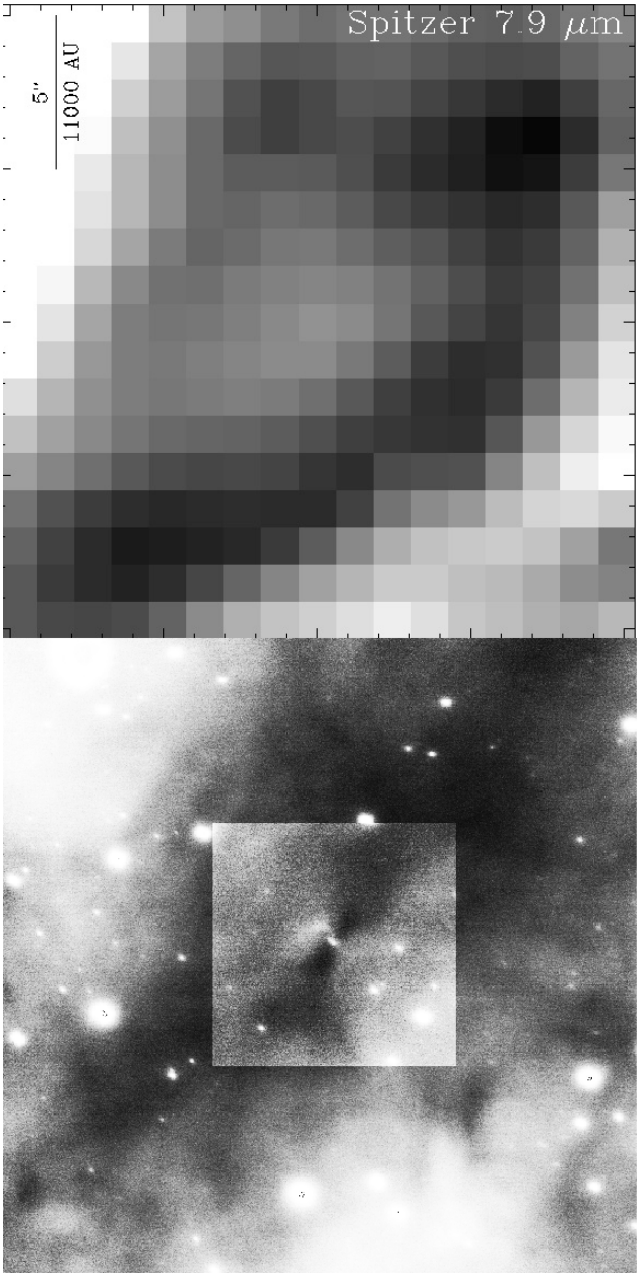

Fig. 11. *Top*: Spitzer image at $\lambda = 7.9$ μm centered at the location of the central object of the silhouette disk. The length scale of 5.″0 is indicated in the upper left corner. *Bottom*: NACO image at $\lambda = 2.2$ μm showing the same region in the M 17. The inner parts are displayed with higher brightness contrast to make the silhouette disk more clearly visible.

account for such a flaring via thermal pressure. The distribution derived in Sect. 3.1 resembles a Maclaurin spheroid at equilibrium, with a shape intermediate between that of a flattened star and of a torus, namely a "hamburger"-type configuration according to the standard classification (e.g. Hachisu & Eriguchi 1984). This structure is typical of low speed, self-gravitating fluids with low-mass central condensation. Indeed, this could indicate that the system is very young and hosts a proto-star with a disk-star mass ratio of the order of 1 and that is accreting material at a high rate. A star much more massive than the cold disk would make it geometrically thin, a situation which does not seem to be met here.

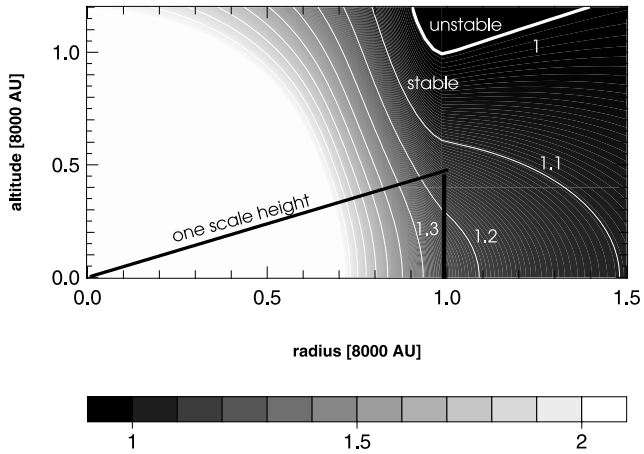

Fig. 12. Ratio of the central to disk gravitational accelerations (vertically), for a disk as massive as the star. The outer edge of the disk is set to 8000 AU. The contour marked with 1 is the stability limit.

The precise knowledge of the radial density profile with a power index close to -1 together with the meridional cross-section of the disk enable however a more quantitative discussion. We have numerically computed the gravitational field due to the disk, using the density splitting method as described in Huré (2005), which yields accurate solutions of the Poisson equation in axially symmetric 3D-systems, for various shapes and density profiles. Figure 12 displays the ratio of the central proto-star gravitational acceleration $g_z^\star$ to the disk's gravity $g_z^{\rm disk}$ in the (r, z)-plane, assuming that the mass contained in the M 17 silhouette and the central mass are equal. In geometrically thin disks, this ratio roughly coincides with the Q-Toomre stability parameter

$$\frac{g_z^\star}{g_z^{\rm disk}} \approx Q = \frac{\Omega c_{\rm s}}{\pi G \Sigma}, \tag{18}$$

where Ω is the rotational velocity, $c_{\rm s}$ is the sound speed, and Σ is the surface density.

Most of our knowledge about the instability of thick disks is derived from numerical simulations by perturbing steady state solutions (Pickett et al. 1996). Assuming, as often done (e.g. Hashimoto et al. 1995), that the stability criterion for thin disks (namely $Q > 1$) applies to thick disks too[1], then Fig. 12 allows for a direct identification of the regions where self-gravity could lead to an unstable structure. First, we see that self-gravity, if not dominant, could play a significant role in the equilibrium of the structure. Second, the space region where $Q < 1$ lies just outside the disk. This means the disk is at the verge of the instability. In other words, self-gravity is important, but not enough to leave the gas unstable. It is then interesting to predict the possible magnitude for the azimuthal rotation velocity of the gas. Approximately, the expected relative deviation from a pure Keplerian rotation is of the order of $M_{\rm disk}(r)/2M_\star$ at a distance r, that is up to 50% for a unit disk to star mass ratio. This deviation, as deduced from the radial component of the gravitational fields (disk and star), is displayed in Fig. 13.

When the disk to central mass ratio $M_{\rm disk}/M_\star$ is increased, the stability limit obviously moves closer to the disk. As α is very close to unity and the aspect ratio is constant, the surface density Σ is almost constant throughout the disk. Hence, the disk

[1] Properties known for thin disks generally hold as long as $h^2 \ll 1$. This means that the Q-stability criterion could be marginally valid here.

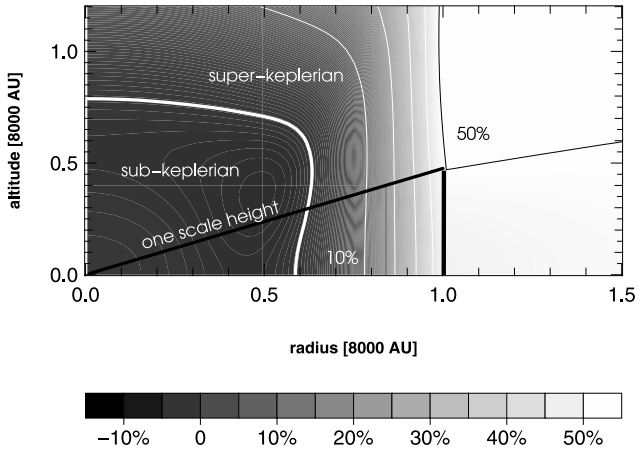

Fig. 13. Possible relative deviation from a pure Keplerian rotation under the same conditions as for Fig. 12 (excluding matter beyond the edge). The bold white line corresponds to the Keplerian value (rotation is faster rightwards of this line).

mass is $\sim\pi\Sigma R^2$. It follows that the disk is stable as soon as the mass ratio $M_{\rm disk}/M_\star > h$, approximately. The condition also reads

$$M_\star < M_\star^{\rm crit} \tag{19}$$

with $M_\star^{\rm crit} = h\ M_{\rm disk}(R)$. The stability of the disk can then be straightforwardly read from Fig. 9 for any central mass.

In Sect. 2.2, we have shown that there is a noticeable degree of point-symmetry in the outer parts of the circumstellar disk. Under the action of self-gravity, the outer disk would show signs of deviation from a Keplerian disk profile (see Fig. 13), and spirals are a possible realization of such distortions (see also Fromang et al. 2004a,b).

For an edge-on disk, such spirals would be seen projected and would only be noticed as a variation in the extinction pattern. The inclination angle of the disk derived from the NACO 2.2 μm image of about 10° might be sufficient to elevate enough of a possible spiral out of the region near the midplane with respect to the line of sight to reveal an "S" – or reversed "S" – shape of the outer structures. A discussion of whether the point-symmetric structure seen in the outer parts is due to large-scale kinematic effects enforced from outside or due to internal effects related to the action of self-gravity, will be given in a subsequent paper.

Information needed to further investigate the density distribution, the star-disk mass ratio, and a possible instability of the disk includes the rotation curve. The position-velocity diagram based on the ^{13}CO 1–0 line data obtained with the Plateau de Bure interferometer presented in Cea04 showed indications for a global rotation of the disk structure, but also a strongly asymmetric pattern, possibly indicating contamination by background material. Moreover, the angular resolution was only about 7.″0 (corresponding to 15 000 AU). Sea05 have re-measured the silhouette structure in the ^{13}CO 1–0 line using the Nobeyama millimeter array with a resolution of about 4.″0 (9000 AU), but have not presented a rotation curve. Future high resolution measurements, possibly using another line, might provide a detailed position-velocity diagram to analyze the kinematic structure present in the circumstellar disk.

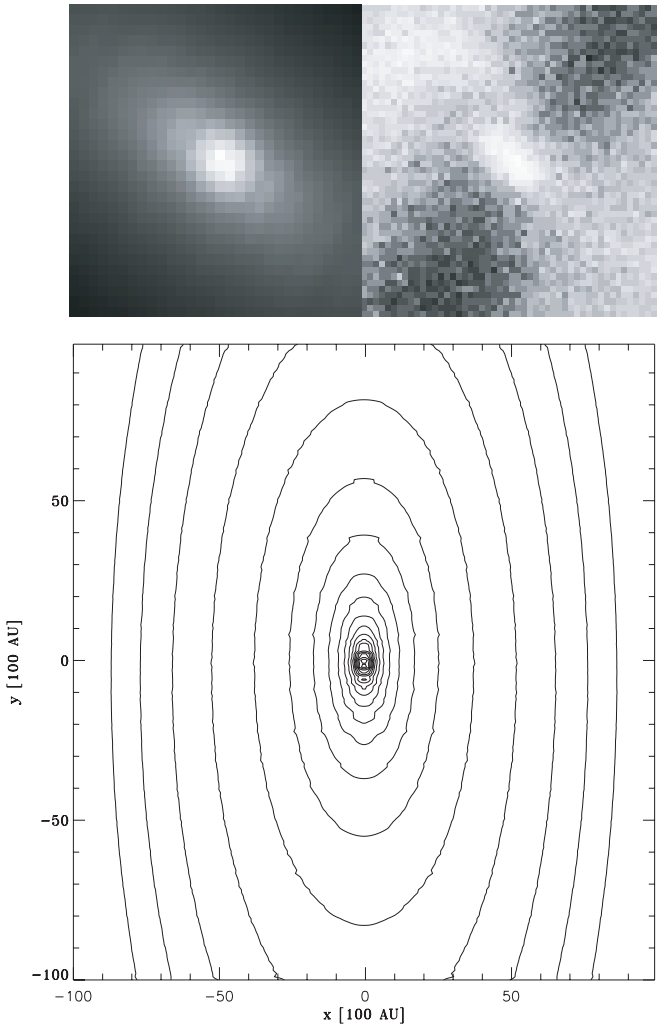

Fig. 14. *Top left image*: theoretical image of the intensity in scattered light propagated from a central point source through the circumstellar disk obtained in the model fit for the inner 3000 AU. The image has been rotated by the angle derived in the fit. *Top right image*: central part of the 2.2 μm NACO image (image extent is 3000 AU). *Bottom plot*: contour plot of the intensity in scattered light propagated from a central point source through the circumstellar disk obtained in the model fit on the large scale. The elliptical shape with an axis ratio close to the ratio of the observed ellipsoidal characterizing the central emission region is visible.

4. Interpretation of the flux received from the central region

It was noted in Cea04 that the nature of the source producing the central peak in the inner 240 × 400 AU of the 2.2 μm-image is difficult to infer. Nevertheless, it is the first case where emission from the center of a massive disk candidate can be seen directly. The region is too small to host a stellar cluster, but a binary system could account for the ellipsoidal shape of the peak. In this section, we will discuss three models for the central emission, and assume for all models a single star as the simplest possible configuration.

At first glance, this would contradict with the ellipsoidal appearance of the central emission region. But this shape can be explained by the scattered light pattern that is caused when the stellar light crosses a flattened structure like the circumstellar disk. Figure 14 displays the results of a radiative transfer calculation using the code described in Steinacker et al. (2003), where a star

is located in the circumstellar disk with the parameters derived in Sect. 3.1. As grains, we assumed again a silicate sphere of size 0.1 μm. The top right image shows the innermost 3000 AU $\times$ 3000 AU from the 2.2 μm NACO image. The top left image is the result of the calculation at the same scale. Note that the pixel scale of the computation was larger than that of the image (100 AU code resolution compared to 60 AU pixel resolution in the NACO image). Also, the rotation of the theoretical image has introduced further errors due to re-binning. The bottom contour plot shows the intensity distribution for a disk that is horizontally oriented and has the same orientation as in Fig. 7. The large-scale intensity structure in scattered light is clearly elliptical. The aspect ratio of the observed and calculated ellipses as well as the orientation in the sky fit very well. The same scattering pattern can also be expected if the central emission is dominated by hot dust in the inner rim of a possible inner disk, which would not be resolved by NACO.

Comparing the ellipsoidal emission pattern in the NACO image and the code results, it appears that the observed emission ellipse is rotated by about 15° clockwise in the sky plane while the theoretical pattern is exactly perpendicular. Two effects might cause this deviation. First, additional emission structures above and below the disk indicate that material might be streaming away from the central region in a complex "jet" pattern. Emission from the jet structure close to the central object would change the central emission, tilting it in the observed direction. Second, a warp of the disk is visible in the outer structure. Referring to Fig. 3, material in the right (left) part is located further up (down). If a fraction of this warping is effective also in the inner parts, it would be barely seen in the extinction analysis, but could lead to a bend of the inner disk giving rise to a rotation of the scattering pattern in the right direction.

For the following estimates, we give here the fluxes and upper flux limits. The flux derived from the 2.2 μm NACO image is 7×10^{-3} mJy and was obtained by adopting and comparing the photometry of three objects listed in the 2MASS database and identified in the NACO FOV. For the wavelengths 3.548 μm, 4.492 μm, and 5.661 μm, upper flux limits of 1.7 mJy, 3.3 mJy, and 8.4 mJy have been deduced from the images of the Spitzer GLIMPSE survey of the galactic plane, respectively. More upper limits could be derived from the observations in the bands B to H presented in Cea04. However, as the extinction is expected to rise for wavelengths smaller than 2.2 μm, these upper limits would not be a constraint on a spectrum derived by assuming certain stellar parameters of the central object. We therefore do not include any limits from these observations in our analysis.

In the following approximate SED fitting, we will neglect the scattering of stellar light into the line of sight in order to be able to perform the SED calculation for many stellar parameters. As the scattered light reaches us through a less dense medium, we underestimate the stellar flux and the derived masses are upper limits.

4.1. Model A: flux of a single star seen through the density distribution of the outer disk

In this model, we assume that the stellar light extinction is caused by the disk part that we have determined from the density fit only. The inner disk radius, which was shown to have little influence on the optical depth, is chosen large enough that the dust particles in the disk are too cold to contribute to the detected emission at 2.2 μm. Further, we assume that the gaseous disk, continuing to smaller radii and being responsible for the accretion signatures, is not massive enough to be seen in the central part of the 2.2 μm image.

The age and the evolutionary stage of the central object is unknown. We therefore have modeled the SED using the stellar radius and temperature as free parameters. For the optical depth derived from the NACO 2.2 μm image, the upper value of 6 was used, resulting in a derivation of upper limits for the stellar mass from our fits. The optical properties of the dust were taken from Draine & Lee (1984) for silicate particles to determine the optical depth in the MIR range with a particle size varying from 0.1 to 1 μm. As the error range for the 2.2 μm-flux, we have used a Gaussian profile with a relative width of 2. The upper limits in the MIR have been incorporated in the fit by assuming a probability of 1 for theoretical SEDs with a value below the limit and a Gaussian decrease with a relative half widths of 2 for values above the limit. The 2.2 μm flux and the flux limits are shown together with the error distributions in gray-scale in the upper left panel of Fig. 15. The total error probability was defined as the sum of all four single error values with equal weighting. For model A, a cut through the error cube containing the three free parameters is shown in the upper right panel of Fig. 15, fixing the particles size at 0.14 μm where the maximum of the error is located. The error is shown as a function of the two other parameters in a gray-scale image where white means probability 1. The dots represent the locations of stellar parameters of a main-sequence star with different masses given in the labels (after Straizys 1992). From this plot, we conclude that assuming extinction of the stellar light by the outer disk only, the central emission seen from the silhouette pattern is consistent with a central main sequence star having a mass of less than 4 $M_\odot$, if the maximal optical depth at 2.2 μm is about 6. The dependencies of the error probability on the dust particle size a are not shown as the derived values depend only weakly on a. This is due to the fact that the optical depth at 2.2 μm is determined from the image independent of a. For larger wavelengths, the optical depths therefore is

$$\tau(\lambda) = \tau(2.2\,\mu\mathrm{m}) \frac{Q_{\mathrm{ext}}^{\lambda}(a)}{Q_{\mathrm{ext}}^{2.2\,\mu\mathrm{m}}(a)} \tag{20}$$

which is almost independent of a for $a \ll \lambda$.

4.2. Model B: flux of a single star seen through the density distribution of an inner and outer disk

If the inner part of the disk extends down to a few stellar radii, the radiative heating by the central star, having mean or even high mass, is likely able to heat the matter above the dust sublimation temperature. This will keep the optical depth of this inner material low compared to the case that dust is present in the gas. Referring to the simulations of Yorke & Sonnhalter (2002), however, it could be argued that the dense inner disk part might be shielded, leaving a substantial amount of dust in the midplane to increase the optical depth for radiation passing this plane (the contribution of the inner disk to the emission will be treated in the model C). In this model, we adopt this assumption and describe the inner disk ranging from the outer radius r_{o} to an inner radius of r_{i} with a disk distribution given in (5), but with changed parameter α_{i}, and h_{i}. We further assume that the dust particles are the same in the inner and outer part, as we refer mainly to cold shielded dust in the midplane.

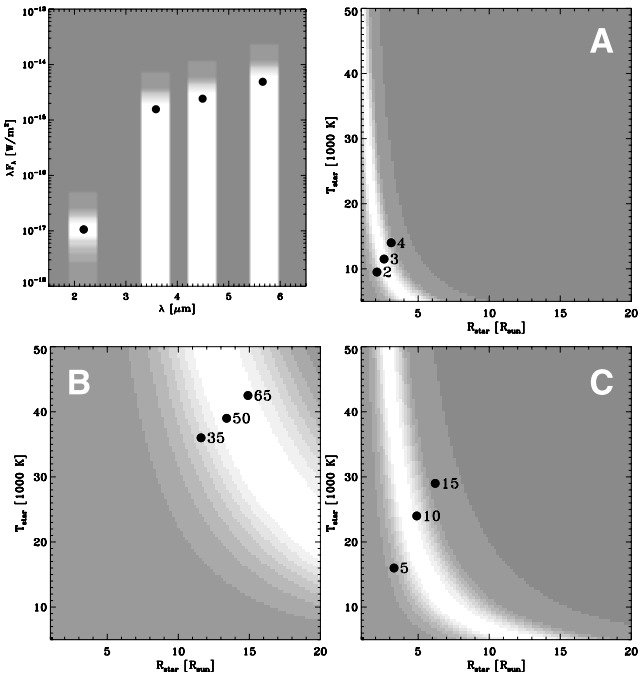

Fig. 15. SED of the central emission region of the massive disk candidate. *Top left*: specific integrated flux density as a function of the wavelengths. The error probability is shown as gray-scale bar with white representing 1. *Top right*: error probability of the SED fit as function of the stellar temperature and radius in gray-scale representation for model A (stellar emission extincted by the outer disk). The dots represent the parameters of main sequence stars where the mass is given as label in $M_\odot$. *Bottom left*: same as top right for model B (stellar emission extincted by the inner and outer disk). *Bottom right*: same as top right for model C (emission from inner disk extincted by the inner and outer disk).

The ratio of the optical depths in the outer disk part τ_o and the inner disk part τ_i is

$$\frac{\tau_\mathrm{i}}{\tau_\mathrm{o}} = \frac{N(r_\mathrm{i}, r_\mathrm{o}, \alpha_\mathrm{i}, h_\mathrm{i})}{N(r_\mathrm{o}, \alpha, h)} = \frac{\alpha - 1}{\alpha_\mathrm{i} - 1} \exp\left[\tan^2 i \left(\frac{1}{h^2} - \frac{1}{h_\mathrm{i}^2}\right)\right]\left[\left(\frac{r_\mathrm{i}}{r_\mathrm{o}}\right)^{1-\alpha_\mathrm{i}} - 1\right]. \quad (21)$$

If we assume a surface density power law with a spectral index of −1.5 like for intermediate-mass Herbig AeBe star models, the corresponding density power law index is $\alpha_\mathrm{i} = 2.5$ (see Dullemond et al. 2001; Semenov et al. 2005). The *e*-folding scale height ratio of the inner disk very much depends on the irradiation of the central star and can vary over the considered radial range. Here, we assume a mean *e*-folding scale height ratio of $h_\mathrm{i} = 0.2$ which is smaller than the outer part value. Already when assuming a small inner disk with an inner radius $r_\mathrm{i} = r_0/3$ (e.g. from 20 to 7 AU), the optical depth defined in (21) increases to a value above 10. Correspondingly, the mass estimates obtained from the SED fit result in a high main sequence stellar masses around 50 $M_\odot$ as visible in the lower left panel of Fig. 15.

4.3. Model C: flux of the inner hot disk seen through the inner and outer disk

There are currently no direction measurements of the emission of massive star/disk systems. The central region of intermediate-mass stars, however, shows a modification compared to the inner region of disks around low-mass stars. From NIR and optical images of intermediate-mass Herbig AeBe stars using ground-based adaptive optics and HST, the central emission seems to be flattened (Grady et al. 2000, 2001; Pantin et al. 2000). On the contrary, from interferometric observations probing the very inner parts, there is little or no evidence for a disklike geometry (Millan-Gabet et al. 2001). The ISO measurements by Meeus et al. (2001) have shown that the emission at 2.2 μm is increased relative to the stellar contribution, and it was argued that this emission can arise from hot dust in the inner parts of a circumstellar disk. As an example, the SED of AB Aur was fitted by Dominik et al. (2003) with a 2.5 $M_\odot$ star and a disk mass of 0.1 $M_\odot$, and a disk-star emission ratio of about 7 at 2.2 μm.

In this model, we assume that the emission from the central region is dominated by the emission of the hot dust in the inner disk by a factor of 7. An inner radius r_i that is a factor of two lower than the radius where the outer disk starts r_0 is used to establish some hot dust close to the star. The fit result is given in the lower right panel of Fig. 15, allowing for main-sequence stellar masses around 10 $M_\odot$.

From applying these three models it is evident that the derived mass of the central object strongly depends on the assumptions about the inner disk due to its edge-on configuration. Further progress towards an unambiguous identification of the inner mass can be expected from future interferometric observations of the inner region or precise rotation curve measurements.

5. Summary and conclusions

In this work, we have analyzed the prominent silhouette structure in M 17 showing a symmetric large-scale pattern in absorption against a bright background, with a central emission region, an hourglass-shaped reflection nebula perpendicular to the extinction bar, a complex outflow over and below the dark extinction lane, and signatures for accretion of matter. Due to the large scale and the strong symmetry of the structure, as well as its presence within a massive star formation region, it attracts special attention as a candidate for a massive disk around a star that might be massive or has the potential to reach such a mass. While the estimate of the disk mass for most massive disk candidates comes from low resolution FIR/mm measurements, we use the advantage that due to the background illumination, the column density can be determined at $\lambda = 2.2$ μm from a high-resolution NAOS/CONICA image.

We investigated wether the observed extinction structure is consistent with a model of a circumstellar rotationally-symmetric flattened density distribution. Applying a commonly used analytical disk model with a powerlaw in radius and a vertical Gaussian distribution, we have fitted a 7 parameter model to the few 8000 pixel of the image. The diffraction limit of the VLT of 0.″056 (*FWHM*) at 2.2 μm is well sampled by the pixel resolution of 0.″027/pixel. Therefore, the PSF of a point source is covered by about 3.3 pixels, corresponding to about 2400 independent data points (the diffraction limit of the VLT is almost reached due to the elimination of the atmospheric disturbance by the adaptive optics system of NACO). We found that the derived optical depth is consistent with a rotationally-symmetric distribution of gas and dust around the central emission peak. The extent of the axis-symmetric disk part is about 3000 AU, with a warped point-symmetrical extension beyond that radius, and therefore larger than any circumstellar disk detected sofar. Surprisingly, we find a flat radial density powerlaw exponent of −1.1 indicating a density distribution with almost constant surface density. The large *e*-folding scale height ratio of about 0.5, however, questions the applicability of

height-integrated quantities and is substantially larger than the *e*-folding scale heights derived for circumstellar disks around intermediate- and low-mass stars.

The disk is seen almost edge-on with an inclination angle of the disk midplane against the sky plane of about 80°. This value is in agreement with the observed symmetry of the hourglass-shaped reflection nebula. If the the confined structures emerging from the central region are interpreted as out-flowing material seen in scattered light, they would be expected to be visible on both sides of the disk for an almost edge-on disk orientation (contrary to a pole-on view where one outflow pattern would dominate the appearance) – and indeed emission from outflow structures can be seen with about equal intensity.

The mass of the entire disk estimated from the column density is discussed depending on the assumed distance and the dust model and ranges between 0.02 and 5 $M_\odot$. We point out that it is essential to give the large range of possible masses reflecting the uncertainties in the background emission flux value, the errors from the model fit, and prominently the uncertainties in the applied dust model. The influence of scattered light on the mass determination is analyzed using 3D radiative transfer calculations. We conclude that unless a star is located close to the disk in the foreground, scattered light will have little influence on the mass determination at 2.2 μm. This has been derived for a homogenous illumination of the disk structure. As the massive stars in M 17 are located northwest of the silhouette filament, this approximation might not hold, but for an inhomogeneous illumination from the side, the effect of scattered light on the mass determination will be less prominent.

The derived disk mass range of 0.02 to 5 $M_\odot$ is smaller than mass range of 110 to 330 $M_\odot$ derived from the ^{13}CO data in Cea04, and compatible with the disk mass estimates from ^{13}CO measurements around 9 $M_\odot$ published in Sea05 (for a distance of 2.2 kpc). As for the determination of the disk mass from interpreting flux differences in NIR images, several assumptions enter the mass determination from line observations of molecules. In the case of measuring ^{12}CO and ^{13}CO, the derived gas mass will depend on the assumptions made to estimate the excitation temperature $T_{\rm ex}$. In particular, the results will vary depending on whether the ^{12}CO emission is treated as optically thick and its temperature is applied as measured in the PdBI data, or whether the ^{12}CO temperature is derived from the ^{13}CO temperature via the ^{12}CO/^{13}CO abundance ratio. The disk mass range found from an LTE calculation for $T_{\rm ex}(^{13}{\rm CO})$ and the opacity $\tau(^{13}{\rm CO})$ defined in Comerón et al. (2005), the estimate for the ^{13}CO column density from Frerking et al. (1982), and the H_2 column density taken from Dickman (1978), is about 2 to 50 $M_\odot$. Without being able to further constrain the disk mass from the currently available data, we note that as in Sea05, the estimated disk masses derived from the NIR extinction are on average lower than the masses based CO line emission analysis.

We present a Spitzer image taken at $\lambda = 7.8$ μm with the disk seen in emission. The emission structure is resolved and elongated, and as scattering is unimportant for 7.8 μm, we identify polycyclic aromatic hydrocarbon emission on the disk surface excited by the nearby massive stars as a possible source of this radiation.

The stability of the disk against self-gravitational forces is analyzed calculating the ratio of the gravitational acceleration by the central object and the disk for the interesting case of equal mass for star and disk. We find that the disk shows deviations only in the outer parts of the disk due to the large *e*-folding scale height factor of about 0.5.

The shape of the central emission regions is analyzed using radiative transfer calculations for a star extinguished by an almost edge-on disk with parameters determined in the column density fit. It is found that the scattered light pattern is elliptical, in agreement with the shape of the central emission region in the NACO 2.2 μm image. We therefore conclude that despite the elliptical shape of the central emission, the central region could host a single star. The same is true if the central emission is dominated by the emission of the unresolved hot dust of the inner disk around a single star.

Estimates of the mass of the central object are given for three models for which we have used further upper flux limits by the Spitzer telescope at MIR wavelengths together with the NACO image to estimate the flux from the central object. Assuming that the optical depth for stellar radiation is determined by the outer disk with little contribution from a possible inner disk, we have varied dust grain size, stellar radius, and stellar surface and find agreement with the flux from a star of several $M_\odot$, if the star has reached the main sequence stage. A model with further extinction from an inner disk with properties like inner disks around intermediate-mass stars leads to mass estimates of the order of 50 $M_\odot$, depending on the assumed inner radius. In a third model where the dominating part of the observed radiation originates from the inner disk (similar to emission from some Herbig AeBe star-disk systems), we estimate the stellar mass to be around 10 $M_\odot$ to be consistent with the observed fluxes.

Thus, our analysis shows that the current observations of the massive disk candidate in M 17 are consistent with a flattened, rotationally-symmetric structure around a central object (or objects). This circumstellar structure is seen almost edge-on and comprises a gas and dust mass of up to 5 $M_\odot$. The disk distribution shows hints of point-symmetrical disturbances in the outer parts. The mass of the central object cannot be constrained rigorously from the existing data due to the edge-on configuration.

Acknowledgements. J.S. thanks the Institute for Pure and Applied Mathematics, UCLA, and the Observatoire de Bordeaux, L3AB, for support and beneficial discussions during visits in 2005. This work was partly funded by the Nordrhein-Westfälische Akademie der Wissenschaften and by the Deutsche Forschungsgemeinschaft, DFG, project number Ts 17/2-1. D.S. is supported by the *Deutsche Forschungsgemeinschaft*, DFG project "Research Group Laboratory Astrophysics" (He 1935/17-2). This work is based on archival data obtained with the Spitzer Space Telescope, which is operated by the Jet Propulsion Laboratory, California Institute of Technology under a contract with NASA. This publication makes use of data products from the Two Micron All Sky Survey, which is a joint project of the University of Massachusetts and the Infrared Processing and Analysis Center/California Institute of Technology, funded by the National Aeronautics and Space Administration and the National Science Foundation. This research has made use of NASA's Astrophysics Data System.

References

Bally, J., & Zinnecker, H. 2005, AJ, 129, 2281
Barber, P., & Hill, S. 1990, in Light Scattering by Particles: Computational Methods (World Scientific Publ. Co Pte Ltd.)
Bonnell, I. A., & Bate, M. R. 2002, MNRAS, 336, 659
Cassen, P., & Moosman, A. 1981, Icarus, 48, 353
Chini, R., Hoffmeister, V., Kimeswenger, S., et al. 2004, Nature, 429, 155
Comerón, F., Schneider, N., & Russeil, D. 2005, A&A, 433, 955
Dickman, R. L. 1978, ApJS, 37, 407
Dominik, C., Dullemond, C. P., Waters, L. B. F. M., & Walch, S. 2003, A&A, 398, 607
Draine, B. T. 1985, ApJS, 57, 587
Draine, B. T., & Lee, H. M. 1984, ApJ, 285, 89
Dullemond, C. P., & Dominik, C. 2004, A&A, 417, 159
Dullemond, C. P., Dominik, C., & Natta, A. 2001, ApJ, 560, 957
Fazio, G. G., Hora, J. L., Allen, L. E., et al. 2004, ApJS, 154, 10

Frerking, M. A., Langer, W. D., & Wilson, R. W. 1982, ApJ, 262, 590
Fromang, S., Balbus, S. A., & De Villiers, J.-P. 2004a, ApJ, 616, 357
Fromang, S., Balbus, S. A., Terquem, C., & De Villiers, J.-P. 2004b, ApJ, 616, 364
Gehrz, R. D., Grasdalen, G. L., Castelaz, M., et al. 1982, ApJ, 254, 550
Grady, C. A., Devine, D., Woodgate, B., et al. 2000, ApJ, 544, 895
Grady, C. A., Polomski, E. F., Henning, T., et al. 2001, AJ, 122, 3396
Greenhill, L. J., Gwinn, C. R., Schwartz, C., Moran, J. M., & Diamond, P. J. 1998, Nature, 396, 650
Hachisu, I., & Eriguchi, Y. 1984, Ap&SS, 99, 71
Hanson, M. M., Howarth, I. D., & Conti, P. S. 1997, ApJ, 489, 698
Hartmann, L., Calvet, N., Gullbring, E., & D'Alessio, P. 1998, ApJ, 495, 385
Hashimoto, M., Eriguchi, Y., & Muller, E. 1995, A&A, 297, 135
Hofner, P., Wiesemeyer, H., & Henning, T. 2001, ApJ, 549, 425
Huré, J.-M. 2000, A&A, 358, 378
Huré, J.-M. 2005, A&A, 434, 1
Marti, J., Rodriguez, L. F., & Reipurth, B. 1993, ApJ, 416, 208
Meeus, G., Waters, L. B. F. M., Bouwman, J., et al. 2001, A&A, 365, 476
Mie, G. 1908, Ann. Phys., 25
Pantin, E., Waelkens, C., & Lagage, P. O. 2000, A&A, 361, L9
Pascucci, I., Wolf, S., Steinacker, J., et al. 2004, A&A, 417, 793
Pickett, B. K., Durisen, R. H., & Davis, G. A. 1996, ApJ, 458, 714
Russeil, D. 2003, A&A, 397, 133
Sako, S., Yamashita, T., Kataza, H., et al. 2005, Nature, 434, 995
Sandell, G., Wright, M., & Forster, J. R. 2003, ApJ, 590, L45
Semenov, D., Pavlyuchenkov, Y., Schreyer, K., et al. 2005, ApJ, 621, 853
Shepherd, D. S., Claussen, M. J., & Kurtz, S. E. 2001, Science, 292, 1513
Steinacker, J., Thamm, E., & Maier, U. 1996, J. Quant. Spec. Radiat. Transf., 56, 97
Steinacker, J., Henning, T., Bacmann, A., & Semenov, D. 2003, A&A, 401, 405
Steinacker, J., Lang, B., Burkert, A., Bacmann, A., & Henning, T. 2004, ApJ, 615, L157
Steinacker, J., Bacmann, A., Henning, T., Klessen, R., & Stickel, M. 2005, A&A, 434, 167
Straizys, V. 1992, in Pachart Astronomy and Astrophysics Series (Pachart Publishing House), 25
Thamm, E., Steinacker, J., & Henning, T. 1994, A&A, 287, 493
Vuong, M. H., Montmerle, T., Grosso, N., et al. 2003, A&A, 408, 581
Werner, M. W., Roellig, T. L., Low, F. J., et al. 2004, ApJS, 154, 1
Wolfire, M. G., & Cassinelli, J. P. 1987, ApJ, 319, 850
Yorke, H. W., & Sonnhalter, C. 2002, ApJ, 569, 846